Island Arc

Island Arc (2013) **22,** 63–73

Thematic Article

Rheological contrast between glaucophane and lawsonite in naturally deformed blueschist from Diablo Range, California

DAEYEONG KIM,[1]* IKUO KATAYAMA,[1] KATSUYOSHI MICHIBAYASHI,[2] AND TATSUKI TSUJIMORI[3]

[1]*Department of Earth and Planetary Systems Science, Graduate School of Science, Hiroshima University, Higashi-Hiroshima 739-8526, Japan (email: daeyeongkim@hiroshima-u.ac.jp),* [2]*Institute of Geosciences, Shizuoka University, Shizuoka 422-8529, Japan, and* [3]*Pheasant Memorial Laboratory, Institute for Study of the Earth's Interior, Okayama University, Misasa, Tottori 682-0193, Japan*

Abstract Deformation microstructures for a lawsonite blueschist from the New Idria serpentinite body, Diablo Range, are investigated to clarify rheological behaviors of glaucophane and lawsonite, which are main mineral assemblages of subducting oceanic crust at relatively cold geotherm. Developments of crystal-preferred orientations (CPOs) with small grain size, irregular grain boundary and high aspect ratio of glaucophane indicate deformation mechanism as recovery and dynamic recrystallization possibly accommodated by dislocation creep, while lawsonite deforms by rigid body rotation based on euhedral grains with angular or straight grain boundaries. Higher aspect ratios, lower angle to foliation, and stronger CPOs of both minerals in the glaucophane-rich layer rather than those in the lawsonite-rich layer suggest the strain localization into the glaucophane-rich layer. Additionally fabric strength (the degree of crystal alignment) and seismic anisotropy are higher in the glaucophane-rich layer than that of the lawsonite-rich layer, which is consistent with the microstructural analyses. All our results imply, therefore, the dominant role of glaucophane rather than lawsonite for rheological behavior and seismic anisotropy of blueschist.

Key words: blueschist, crystal-preferred orientation, glaucophane, lawsonite, rheological contrast, strain localization.

INTRODUCTION

Investigations on strength contrast among minerals or competence contrast among layers can be important to aid understanding of geological problems such as the depth of earthquakes and viscous coupling between the crust and mantle. Especially in subduction zones, dehydration of hydrous phases and formation of high-pressure minerals occur with high stress regimes. Those phenomena are crucial for the comprehension of crust–mantle circulations.

Blueschist usually forms at low-temperature and high-pressure conditions by the subduction and metamorphism of oceanic crust originating from mid-ocean ridge basalt (MORB). High-pressure minerals, such as glaucophane and lawsonite, can be preserved as an inclusion or a matrix, which might form during subduction or exhumation, respectively. Although dissolution–precipitation creep is one of the dominant deformation mechanisms of calcic amphibole at low temperature (e.g., Imon *et al.* 2004), rigid-body rotation (Ildefonse *et al.* 1990), dislocation creep with recovery (Reynard *et al.* 1989), and dynamic recrystallization (Zucali *et al.* 2002) are also possible deformation mechanisms of natural glaucophane deformed at relatively high pressures. Deformation mechanisms and slip systems of glaucophane during the retrograde stage, however, are poorly understood.

We therefore conducted fabric analyses of lawsonite blueschist from the New Idria serpentinite body of the Diablo Range, California, USA, to delineate the rheological behaviors of subducting

*Correspondence.

Received 28 February 2012; accepted for publication 19 July 2012.

doi:10.1111/iar.12003

oceanic crust. The body underwent a blueschist-facies overprint during exhumation (Tsujimori *et al*. 2007), and therefore represents the rock that was deformed during the retrograde process. The deformation conditions might be similar to those of subduction (especially in the case of grain size), and the deformation mechanisms and relative strength between glaucophane and lawsonite are discussed.

SAMPLE DESCRIPTION

GEOLOGICAL OUTLINE

The New Idria serpentinite body in the Diablo Range, a part of the Coalinga anticline, borders the Upper Cretaceous Panoche and Moreno Formations of the Great Valley Group and Franciscan Complex. The body containing numerous tectonic blocks of greenstone and low-grade blueschists comprises primary chrysotile-lizardite serpentinite and minor antigorite serpentinite which was a moderately depleted harzburgite based on chemical compositions of relict minerals (Coleman 1980; Tsujimori *et al*. 2007). The presence of high-grade tectonic blocks composed of retrograded eclogite and garnet amphibolite indicates the origin of the New Idria serpentinite from mantle depth (Tsujimori *et al*. 2007). The investigated lawsonite blueschists were collected as a boulder at near eclogite locality along the Clear Creek (Fig. 1).

MINERAL ASSEMBLAGES AND TEXTURES

In this study, we selected a sample, which contains two distinctively representative parts, a glaucophane-rich layer (GRL) and a lawsonite-rich layer (LRL), on the basis of mineral abundances (Fig. 2). This helps to clarify the rheological contrast between glaucophane and lawsonite, and its effects on active slip systems and seismic anisotropy of subducting oceanic crust. The GRL comprises primarily glaucophane (89%), lawsonite (8%), and rare phengite around lawsonite with minor accessory minerals (titanite and apatite) (Fig. 2a,c). Glaucophane as a main component of the matrix is highly foliated and elongated with very

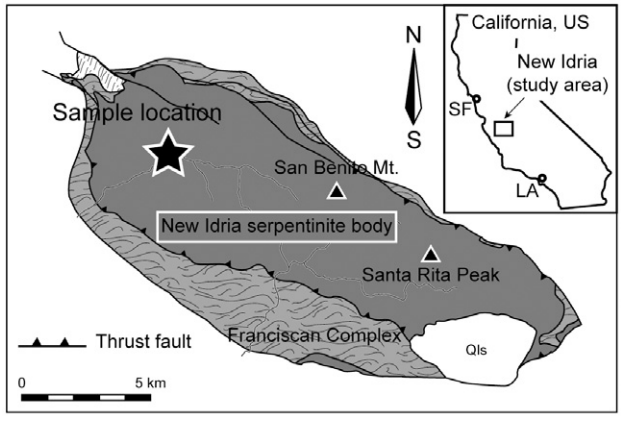

Fig. 1 Simplified geologic map and the sample location. See Tsujimori *et al.* (2007) and Coleman (1996) for a larger-scaled map. Qls: Holocene-Pleistocene alluvium; SF, San Francisco; LA, Los Angeles.

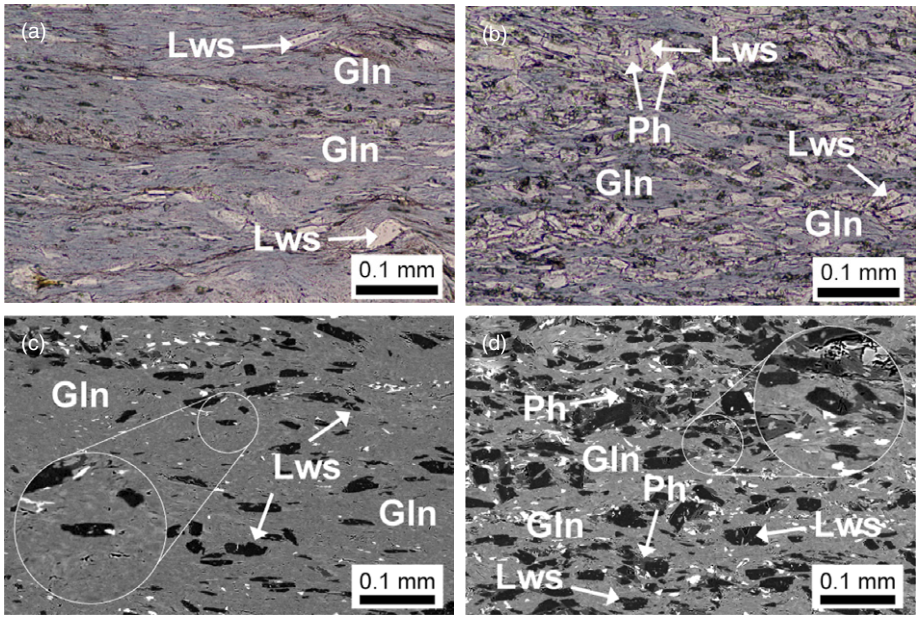

Fig. 2 Photomicrographs and back-scattered electron images (BSEI) of two representative domains. (a) and (c) show the glaucophane-rich layer defined by abundant glaucophane (89%), lawsonite (8%) and rare phengite, while (b) and (d) display the lawsonite-rich layer characterized by high concentrations of lawsonite (21%) partly wrapped by secondary phengite (dark grey in BSEI). Enlarged figures show euhedral grain shape or straight grain boundaries of lawsonite. Lws, lawsonite; Gln, glaucophane; Ph, phengite. Mineral abbreviations follow Whitney and Evans (2010).

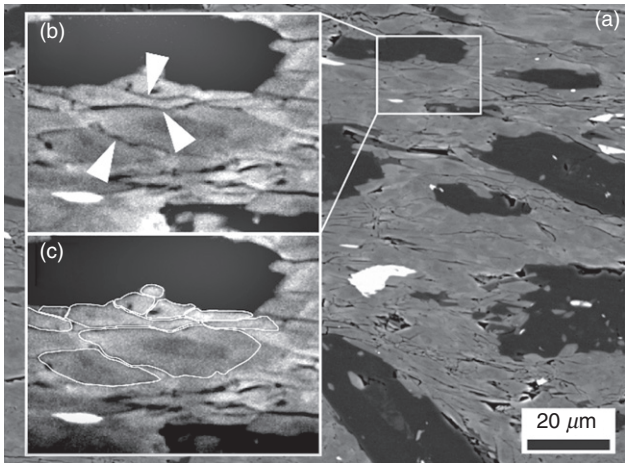

Fig. 3 Microstructures of glaucophane. (b) and (c) show the enlarged rectangle in (a). Sharp apexes of triangles indicate curved or irregular grain boundary of glaucophane. (c) displays an example for the image analyses.

fine grain size, suggesting the possible formation of glaucophane during the exhumation process. Often an irregular grain boundary of glaucophane is observed (Fig. 3). Lawsonite having subhedral to euhedral shape with straight grain boundaries is preserved as porphyroclasts wrapped mostly by glaucophane. The LRL chiefly comprises glaucophane (64%), lawsonite (21%) and secondary phengite (11%) enclosing lawsonite (Fig. 2b,d). Grain sizes of minerals in the LRL are somewhat larger than those in the GRL.

MINERAL CHEMISTRY

Major elements of these minerals were measured using the JEOL JXA-8200 (EPMA), housed at Hiroshima University. We employ the average of maximum and minimum estimates on the basis of total cations as 13 for T- and C-sites, and 15 for T-, C- and B-sites, respectively, for the contents of ferric iron in amphibole (Table 1) (Leake *et al.* 1997). All sodic amphiboles ($^{[B]}Na \geq 1.5$) in both GRL and LRL are classified as glaucophane by definitions such as $(Na + K)_A < 0.50$, $Mg/(Mg + Fe^{2+}) \geq 0.5$, and $^{6}Al \geq Fe^{3+}$ (Fig. 4). Only a few grains in the LRL have core-rim structures characterized by the increase of $Fe^{3+}/(Fe^{3+} + {}^{[6]}Al)$, defining tschermkite substitution, and the decrease of Al and Na contents from core to rim, classifying the rim composition as winchite or actinolite (Fig. 4). The decrease of Al content from the core to the rim suggests the formation of amphibole during the retrograde stage, due to the systematic correlation between pressure and Al_2O_3 content of sodic amphibole (Maruyama *et al.* 1986). In addition, mineral assemblages (Gln + Lws + Ph + Ttn) are similar to those in blueschist-facies overprinting stage of high-grade blocks from New Idria (Tsujimori *et al.* 2007), except the lack of jadeite. We therefore adopt temperature ranges of 200–290°C for pumpellyite-zone metabasites (Maruyama & Liou 1988) and pressure ranges >1.0 GPa for the Jd + Qz stability field (Tsujimori *et al.* 2007) in this sample.

MICROSTRUCTURAL AND FABRIC ANALYSES

Measurements of aspect ratios, angle to the foliation, and grain size for minerals in XZ sections (the plane perpendicular to the foliation and parallel to the lineation) of the GRL and LRL were conducted by an image-analysis software ImageJ 1.44, in which best-fit ellipses for each grain were computed for reducing the complexity of various shapes (Fig. 3c) (e.g., Mezger 2010). Aspect ratios of glaucophane in each domain are distinctively diverse (12.8 average in the GRL and 6.0 in the LRL), in contrast to relatively similar results of aspect ratios in lawsonite (5.0 average in the GRL and 3.6 in the LRL) (Fig. 5, Table 2). Angles to the foliation of glaucophane in both layers exhibit almost similar results within 30°, while lawsonite in the LRL shows more scattered patterns than that in the GRL. The grain size of glaucophane in the GRL (7 μm mean value) is smaller than that in the LRL (12 μm), while distributions of grain size for lawsonite are comparable (18 μm in the GRL and 20 μm in the LRL) (Fig. 5, Table 2).

The Kikuchi bands were acquired for XZ sections and analyzed using the HKL–EBSD system attached to the Hitachi S-3400N at Shizuoka University. To unravel the effects of chemical zonings in glaucophane and lawsonite, automatic mappings (1 μm step size) for each domain were carried out. After we confirmed identical crystallographic orientation throughout the whole grain, the EBSD patterns were manually indexed. Pole figures were plotted using the software PFctf, made by D. Mainprice and J- and M-indexes were employed for estimating fabric strength (Mainprice & Silver 1993; Ismaïl & Mainprice 1998; Skemer *et al.* 2005). As a result, glaucophane and lawsonite in both layers have certain similar crystal-preferred orientations (CPOs) for each mineral except for slightly scattered patterns in the LRL. Glaucophane exhibits the [001] axes parallel to the

Table 1 Representative chemical compositions of minerals in each layer

Area	Gln-rich layer						Lws-rich layer						
Phase	Gln			Lws		Ph	Gln				Lws		Ph
Spot no.	14	16	1	5	6	4	33	40	48c†	49r‡	79	80	17
SiO_2	56.05	56.05	56.13	38.36	37.67	52.45	55.86	56.77	56.09	56.00	37.92	37.66	52.86
TiO_2	0.00	0.03	0.03	0.03	0.13	0.03	0.08	0.08	0.06	0.05	0.09	0.19	0.06
Al_2O_3	8.12	7.21	8.54	31.55	30.95	24.19	8.01	8.40	9.28	6.87	30.90	31.12	23.11
Cr_2O_3	0.00	0.06	0.03	0.00	0.07	0.10	0.00	0.04	0.05	0.08	0.02	0.05	0.08
FeO	16.12	16.21	15.94	1.48	0.97	3.79	14.81	15.20	14.71	15.54	1.31	0.96	3.27
MnO	0.09	0.16	0.12	0.00	0.02	0.06	0.08	0.09	0.06	0.25	0.01	0.00	0.02
MgO	8.33	8.84	7.87	0.01	0.05	4.22	8.79	8.66	8.14	9.32	0.04	0.02	4.73
CaO	1.06	2.16	0.62	17.33	17.08	0.03	0.65	0.74	0.56	2.80	16.78	17.09	0.03
Na_2O	7.09	6.46	7.25	0.00	0.01	0.15	7.10	7.37	7.42	6.15	0.02	0.00	0.07
K_2O	0.00	0.00	0.02	0.01	0.01	10.76	0.00	0.02	0.02	0.10	0.02	0.02	10.80
P_2O_5	0.00	0.00	0.00	0.00	0.00	0.00	0.00	0.00	0.00	0.00	0.00	0.00	0.00
Total	96.86	97.16	97.53	88.77	86.96	95.79	95.36	97.37	96.38	97.14	87.12	87.09	95.04
O.N.	23.00	23.00	23.00	8.00	8.00	11.00	23.00	23.00	23.00	23.00	8.00	8.00	11.00
Si	7.96	7.96	7.98	2.01	2.02	3.51	7.99	7.97	7.95	7.96	2.02	2.01	3.56
Ti	0.00	0.00	0.00	0.00	0.01	0.00	0.01	0.01	0.01	0.01	0.00	0.01	0.00
Al	1.36	1.21	1.43	1.95	1.95	1.91	1.35	1.39	1.55	1.15	1.94	1.96	1.83
Cr	0.00	0.01	0.00	0.00	0.00	0.01	0.00	0.00	0.01	0.01	0.00	0.00	0.10
Fe^{3+}§	0.45	0.43	0.43	0.07	0.04		0.46	0.46	0.36	0.41	0.06	0.04	
Fe^{2+}	1.91	1.93	1.90			0.21	1.77	1.78	1.74	1.85			0.18
Mn	0.01	0.02	0.01	0.00	0.00	0.00	0.01	0.01	0.01	0.03	0.00	0.00	0.00
Mg	1.76	1.87	1.67	0.00	0.00	0.42	1.88	1.81	1.72	1.97	0.00	0.00	0.47
Ca	0.16	0.33	0.09	0.97	0.98	0.00	0.10	0.11	0.08	0.43	0.96	0.98	0.00
Na	1.95	1.78	2.00	0.00	0.00	0.02	1.97	2.01	2.04	1.69	0.00	0.00	0.01
K	0.00	0.00	0.00	0.00	0.00	0.92	0.00	0.00	0.00	0.02	0.00	0.00	0.93
P	0.00	0.00	0.00	0.00	0.00	0.00	0.00	0.00	0.00	0.00	0.00	0.00	0.00
Total	15.11	15.10	15.09	5.01	5.00	7.00	15.08	15.10	15.11	15.11	5.00	5.00	6.99
gln	0.73	0.65	0.77				0.74	0.75	0.82	0.62			
mrb	0.25	0.24	0.23				0.25	0.25	0.20	0.23			
act	0.31	0.64	0.19				0.20	0.22	0.17	0.83			
ts	0.00	0.00	0.00				0.00	0.00	0.00	0.00			

† Including core compositions. ‡ Denoting rim compositions. § Employing the average of maximum and minimum ferric iron contents in glaucophane (Leake *et al*. 1997).

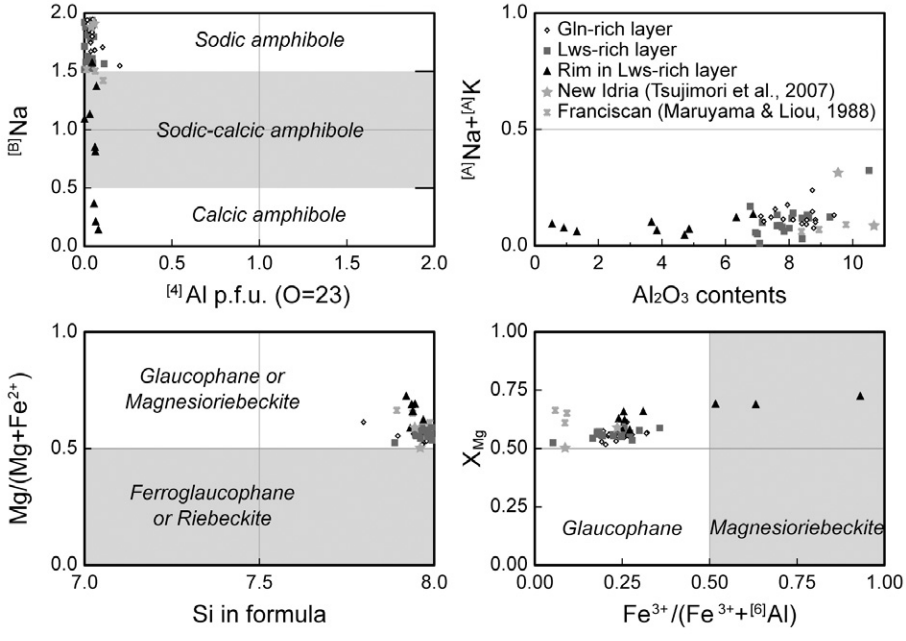

Fig. 4 Chemical compositions of amphibole. The contents of ferric iron in amphibole were calculated as the average of maximum and minimum estimates based on total cations as 15 for T-, C- and B-sites and 13 for T- and C-sites. Major elements of amphiboles in New Idria (Tsujimori *et al*. 2007) and those in the Franciscan complex (Maruyama & Liou 1988) were also marked for comparisons.

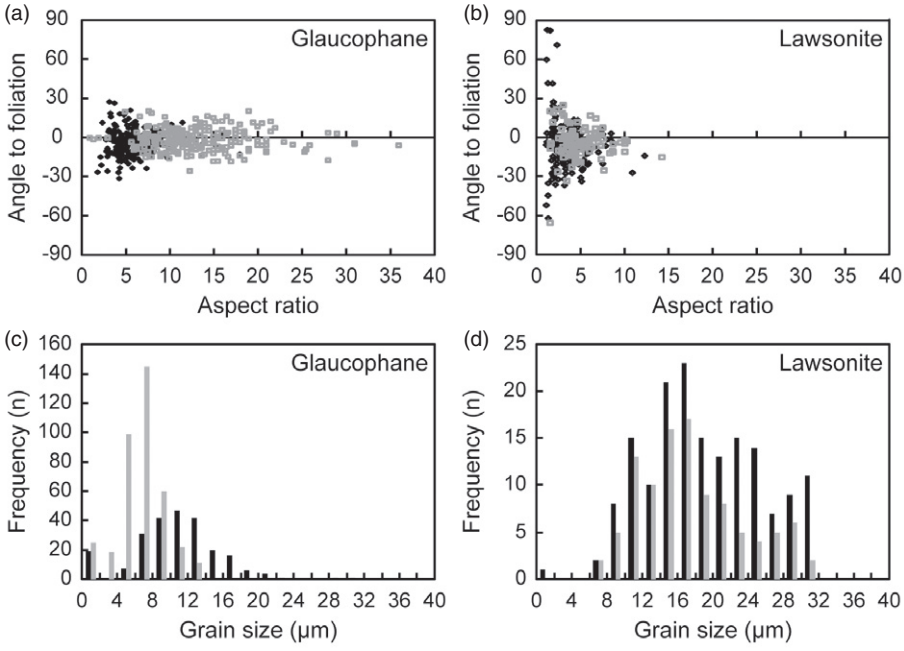

Fig. 5 Diagrams of the angle to foliation against aspect ratio, and the frequency of grain size calculated by ImageJ 1.44 (http://rsb.info.nih.gov/ij/). Best-fit ellipses were employed for diminishing the complexity of diverse shapes. Angles to foliation of (a) glaucophane: □, Gln-rich layer (n = 236); ◆, Lws-rich layer (n = 237), and (b) lawsonite: □, Gln-rich layer (n = 103); ◆, Lws-rich layer (n = 171). Grain sizes of (c) glaucophane: ■, GRL (n = 236); ■, LRL (n = 237); and (d) lawsonite; ■, GRL (n = 103); ■, LRL (n = 171).

Table 2 Comparisons of glaucophane and lawsonite in two dominant layers

Domain	Modal abundance†	Minerals	Grain size (μm)	Aspect ratio (with standard deviation)	Fabric strength	Seismic anisotropy AV_P	Seismic anisotropy AV_S
Gln-rich layer	Gln89 Lws8	Gln	7	12.8 ± 6.4	M = 0.20, J = 18.0	25.3%	13.9%
		Lws	18	5.0 ± 2.3	M = 0.21, J = 9.6	10.7%	21.3%
Lws-rich layer	Gln64 Lws21	Gln	12	6.0 ± 2.8	M = 0.18, J = 16.0	20.2%	9.9%
		Lws	20	3.6 ± 1.5	M = 0.15, J = 7.8	8.8%	19.4%

† Excluding phengite, titanite and apatite (abundances of each mineral are less than 5%).

lineation, the (100) planes vertical to foliation plane, and relatively weak central maxima in the (010) planes (Fig. 6a,c). Glaucophane in the GRL (M = 0.20, J = 18.0) displays higher fabric strength than that in the LRL (M = 0.18, J = 16.0) (Fig. 6 and Table 2). The CPOs of lawsonite are characterized by vertical maxima in the [001] axes, horizontal maxima in the [010] axes, and weak patterns in the [100] axes (Fig. 6b,d). M- and J-indexes of lawsonite in the GRL are estimated as M = 0.21 and J = 9.6, while those in the LRL are M = 0.15 and J = 7.8 (Fig. 6 and Table 2).

We computed the seismic properties of glaucophane and lawsonite in the GRL and LRL. The seismic anisotropy of P-wave (AV_P) is defined by the maximum and minimum velocities in two different propagating paths, hence the percentage AV_{Pmax} can be calculated using the formula $200(V_{Pmax} - V_{Pmin})/(V_{Pmax} + V_{Pmin})$. The S-wave anisotropy (AV_S) is described as two different velocities of two orthogonally polarized S-waves separately propagated through an anisotropic medium, therefore the percentage AV_{Smax} is calculated by the formula $200\ (V_{S1} - V_{S2})/(V_{S1} + V_{S2})$, in which V_{S1} and V_{S2} are faster and slower velocities, respectively. The elastic constants (C_{ij}) of glaucophane (Bezacier *et al.* 2010) and lawsonite (Sinogeikin & Bass 2000) are employed for calculating seismicity of crystals with the Voigt–Reuss–Hill averaging scheme. The V_P, AV_S and orientation of V_{S1} polarization of glaucophane and lawsonite in both layers are projected to lower hemispheres (Fig. 7). Seismic velocities in the GRL are V_P 6.73–8.68 km/s, V_{S1} 4.34–4.93 km/s and V_{S2} 4.27–4.57 km/s for glaucophane with strong anisotropy (AV_{Pmax} = 25.3% and AV_{Smax} = 13.9%) and V_P 7.68–8.55 km/s, V_{S1} 4.11–4.55 km/s and V_{S2} 3.64–4.29 km/s for lawsonite with P- and S-wave seismic anisotropy as 10.7% and 21.3%, respectively (Fig. 7a,b). The V_P, V_{S1} and V_{S2} in the LRL are calculated to 7.15–8.74 km/s, 4.52–4.82 km/s and 4.29–4.60 km/s for glaucophane (AV_P = 20.0% and AV_S = 9.9%) and 7.65–8.35 km/s, 3.93–4.56 km/s,

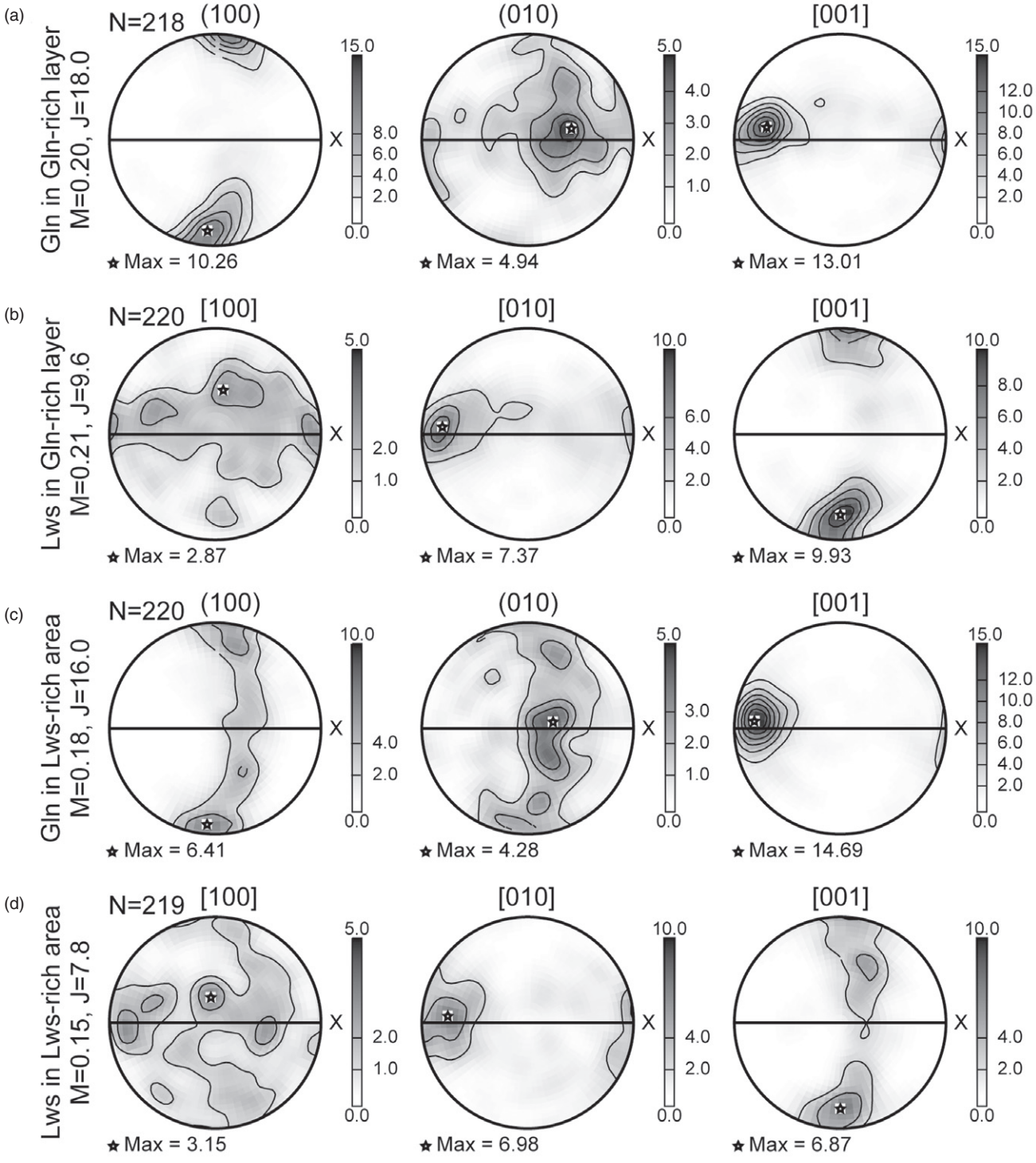

Fig. 6 Pole figures of glaucophane and lawsonite in glaucophane-rich (a and b) and lawsonite-rich (c and d) layers. Poles were plotted employing equal-area projection in lower hemisphere. Density of poles was expressed as contours by the multiples of uniform distribution (m.u.d.). The bold line in the middle of poles and *X*-axis presents the directions of foliation and lineation, respectively.

3.74–4.19 km/s for lawsonite ($AV_P = 8.8\%$ and $AV_S = 19.4\%$), respectively (Fig. 7c,d). The V_{Pmax} of glaucophane in both layers is developed along the lineation parallel to the [001] axes and the AV_{Smax} and V_{S1max} polarization are established as girdle type along the foliation perpendicular to the (100) planes in CPOs, while lawsonite shows V_{Pmax} normal to the foliation associated with the [001] axes and AV_{Smax} and V_{S1max} polarization in central maxima.

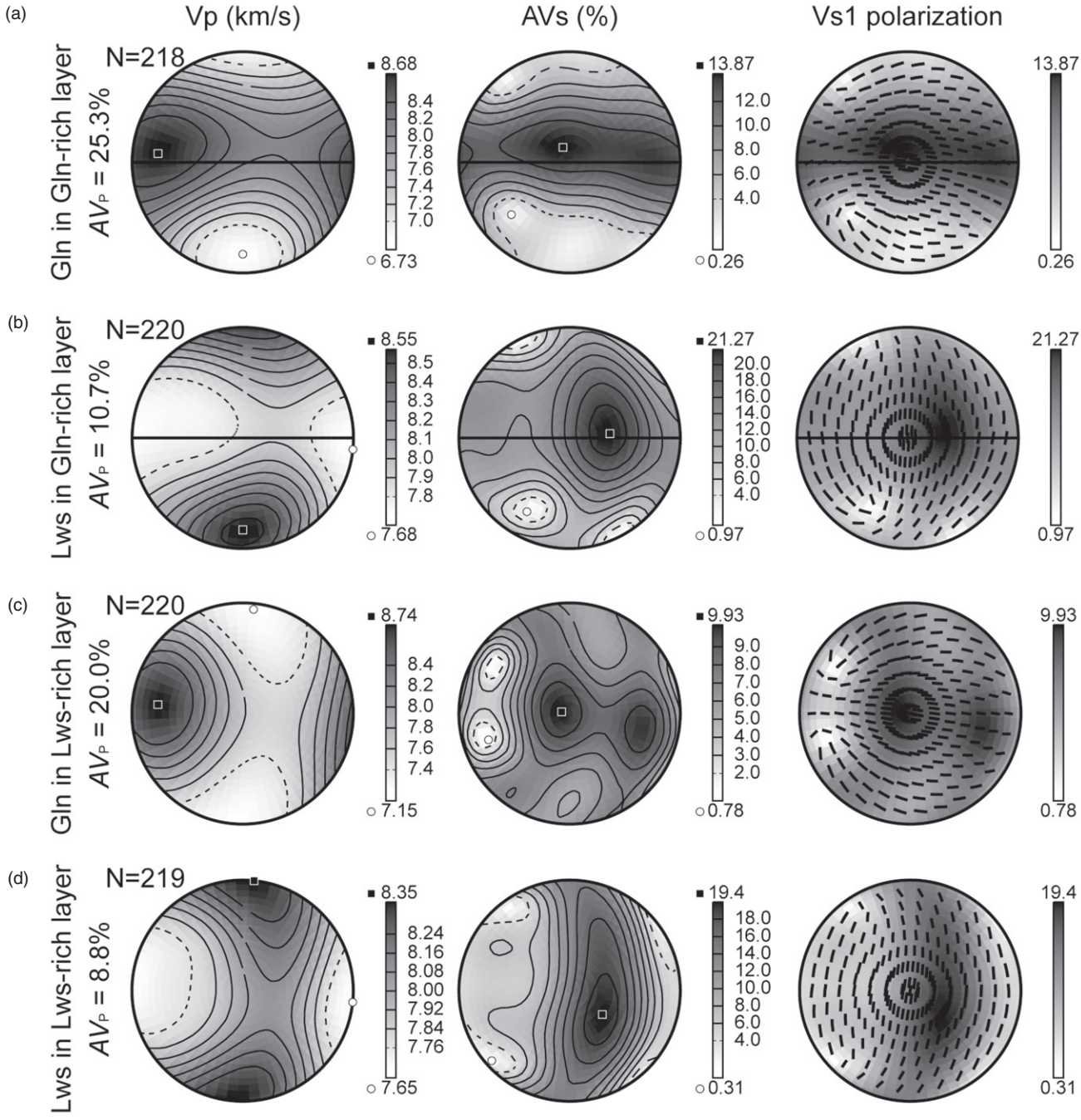

Fig. 7 Computed seismic anisotropy of glaucophane (a, c) and lawsonite (b, d) in the glaucophane-rich and lawsonite-rich layers, respectively. Equal area projection and the Voigt–Reuss–Hill averaging scheme were employed in lower hemisphere.

DISCUSSIONS

DEFORMATION MECHANISMS OF GLAUCOPHANE AND LAWSONITE

Microstructural investigations suggested cataclastic deformation (Nyman *et al.* 1992), rigid-body rotation (Ildefonse *et al.* 1990; Siegesmund *et al.* 1994), and dynamic recrystallization (Cumbest *et al.* 1989) as possible deformation mechanisms of natural amphibole. Glaucophane is a relatively weak mineral among amphiboles, attributed to diverse slip systems and an inclination for recovery and recrystallization processes (Reynard *et al.* 1989; Zucali *et al.* 2002). In addition, small grain size is normally attributed to strain-induced recrystallization during or after crystal plastic deformation (e.g., Drury & Urai 1990).

Glaucophane in the analyzed samples shows small grain size (possibly owing to grain size reduction) and well-developed CPOs normally considered as products of dynamic recrystallization (Díaz Aspiroz *et al.* 2007). The result can be also supported by the grain size distribution of glaucophane into <2 μm and 4–22 μm for the LRL, and possibly <2 μm and 4–14 μm for the GRL (Fig. 5). Glaucophane is, therefore, likely to have been deformed by recovery and dynamic recrystallization mechanisms, perhaps accommodated by dislocation creep. Irregular or curved grain boundaries of glaucophane designate the presence of annealing and grain growth ascribed to the reduction of interfacial free energy in a low stress regime (Fig. 3b) (Evans *et al.* 2001). Dissolution and precipitation creep can be operated under low temperatures in the presence of aqueous fluids; however, this may not be the main controlling mechanism for the analyzed sodic amphiboles because of the stronger fabric for fine-grained glaucophane and weak chemical zoning, whereas calcic amphiboles are deformed by dissolution and precipitation, as evident by shape preferred orientation and clear chemical zoning (e.g., Imon *et al.* 2004). The deformation mechanism of lawsonite, on the other hand, is poorly understood. Lawsonite in the sample also exhibits relatively strong CPOs, however, grains are euhedral with angular or straight boundaries and are partly wrapped by phengite (Fig. 2). The wide range of the stability field of lawsonite with these microstructures intimates that the predominant deformation mechanism is likely to be rigid body rotation.

DEFORMATION CONDITIONS FOR THE DIABLO RANGE BLUESCHIST

Lawsonite eclogite normally occurs at deeper than 45 km depth in subduction zones (Tsujimori *et al.* 2006), nevertheless its exhumation to the surface is rare without alteration. The Diablo Range exceptionally maintains unaltered lawsonite eclogite, implying rapid exhumation probably due to slab breakoff. Lawsonite in the analyzed sample might have been formed during prograde metamorphism and suffered the maximum pressure condition (1.3 GPa) of the New Idria serpentinite body (Tsujimori *et al.* 2007). On the other hand, glaucophane may have appeared during a retrograde *P–T* path based on the chemical compositions of the core (glaucophane) and rim (winchite or actinolite). The strongly aligned grains for both lawsonite and glaucophane are proved by low degrees of angle to the foliation (Fig. 5), indicating the presence of deformation during or after the blueschist-facies overprinting. The development of CPO might be imputed to the flow of dynamically recrystallized small grains, suggesting syn-kinematic microstructures. Consequently the main deformation event that formed these microstructures occurred at temperatures ranging from 200 to 290°C and pressures over 1.0 GPa (Tsujimori *et al.* 2007). The deformation at a relatively high pressure may cause the operation of plastic deformation in sodic amphibole rather than the cataclastic deformation.

RHEOLOGICAL CONTRAST BETWEEN GLAUCOPHANE AND LAWSONITE

Deformation is generally concentrated into specifically weak minerals or layers (e.g., Ebert *et al.* 2007), therefore the strength contrast between glaucophane and lawsonite against deformation can help to understand the rheology of the subducting slab. For examining this concept, we assume that the analyzed rock is composed only of two phases, glaucophane and lawsonite. Microscopic observations designate that grains of glaucophanes and lawsonite in the GRL are comparatively small compared with those in the LRL (Fig. 2). The results of image analyses for glaucophane and lawsonite in the GRL intimate higher aspect ratios, larger grain size, and alignment of the longaxes along foliation than those in the LRL (Fig. 5). Higher fabric strength in the GRL is also revealed based on M- and J-indexes, which is corresponding to aspect ratio (Fig. 8 and Table 2). All evidence demonstrates that strain is localized into the GRL rather than the LRL, denoting glaucophane as weaker than lawsonite against deformation. Our study, therefore, proves that the rheology of subducting oceanic crusts can be primarily influenced by glaucophane. This is in agreement with the results of Teyssier *et al.* (2010) who reported lawsonite vorticity owing to the treatment of lawsonite and glaucophane as a rigid grain and a ductile matrix, respectively.

SLIP SYSTEMS AND SEISMIC ANISOTROPY

Slip systems are usually managed by physical variables such as pressure (*P*), temperature (*T*), stress (strain or strain rate), and water fugacity (Carter & Avé Lallemant 1970; Jung & Karato 2001; Jung *et al.* 2006). The sample analyzed experienced almost comparable histories for *P*, *T*, and water

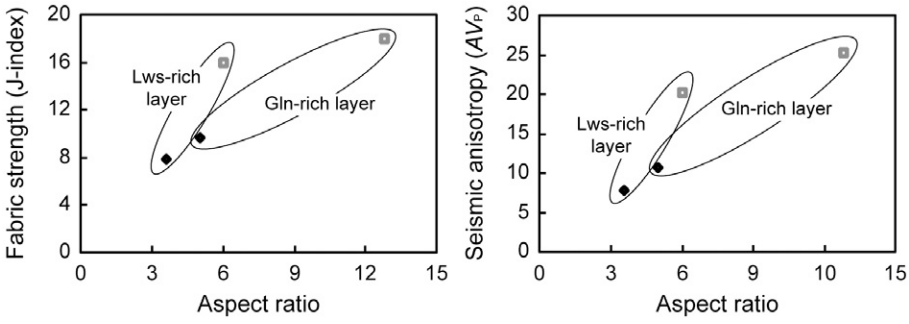

Fig. 8 Comparisons of fabric strength, seismic anisotropy and aspect ratio. Calculations of fabric strength (J-index) follow Mainprice and Silver (1993) and P-wave seismic anisotropy was computed using the software ANISctf made by D. Mainprice. □, Gln; ◆, Lws.

fugacity hence, in this study, strain could be the only concern for slip systems of glaucophane in the GRL and the LRL. Pole figures of glaucophane show vertical maxima in the (100) planes and horizontal maxima in the [001] axes, insinuating slip plane and direction, respectively (Fig. 5a,c). The results advocate that the strength of stress or strain can scarcely influence the slip systems of glaucophane. Duplicate glaucophane LPOs, which can be used for estimating the slip system, are reported for lawsonite blueschists deformed at 2 GPa and 430°C (Teyssier *et al.* 2010) and at 0.7–0.9 GPa and <350°C (Fujimoto *et al.* 2010). These reveal the same slip systems as glaucophane in diverse *P–T* conditions when other factors (strain and water fugacity) are fixed, therefore glaucophane possibly has identical slip systems during both subduction and exhumation.

The CPOs of lawsonite show the [010] axis subparallel to the lineation and the [001] axis normal to the foliation, possibly developed by solid body rotation (Fig. 5b,d). This pattern is different from that reported in lawsonite, (100)[001] (Teyssier *et al.* 2010) and (001)[100] (Fujimoto *et al.* 2010). These disagreements are probably attributable to the difference in deformation mechanism, deformational P–T conditions, or degree of rotation, nevertheless strain rate, stress (or strain), and water fugacity should also be contemplated.

To evaluate impacts of strain localization on seismic anisotropy, we computed the seismic properties of glaucophane and lawsonite in the GRL and LRL (Fig. 7). The degree of seismic anisotropy of glaucophane and lawsonite in the LRL are relatively low compared with those in the GRL, in agreement with the aspect ratios and fabric strengths (Fig. 7 and Table 2). Those are mainly caused by strain localization, because they were calculated from CPOs. However glaucophane and lawsonite have different CPOs, therefore seismic anisotropy of the rock masses were computed in order to comprehend the effects of mineral abundances (Fig. 9) (Mainprice *et al.* 2000). The highest AV_{Pmax} for the GRL and LRL were calculated as 20.0 and 25.3%, respectively, for the rock comprising 100% glaucophane, while the highest AV_{Smax} were 19.4 and 21.3%, respectively, for the rock containing 100% lawsonite. The lowest AV_{Pmax} and AV_{Smax} are modeled as the rock composed of 70% glaucophane and 30% lawsonite for AV_P, and of 30% glaucophane and 70% lawsonite. The distinctive 'concave' feature is probably attributable to directions of seismic anisotropy originating from CPOs (Figs 6,7). Consequently we denote here that seismic anisotropy of a rock mass, especially one composed of highly anisotropic phases, is controlled by the abundance of rock-forming minerals.

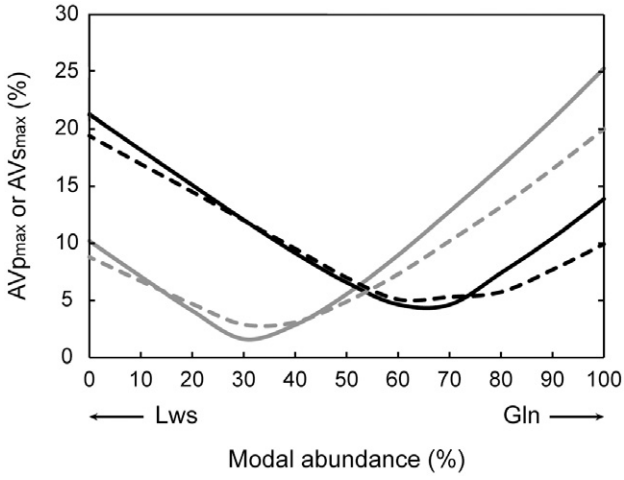

Fig. 9 A graph for P- and S-wave seismic anisotropy according to modal abundance. The AV_P of both layers is the strongest for the rock composed of 100% glaucophane, decreases with the increase of lawsonite abundance, and finally reaches to minimum value when the rock comprises 30% of glaucophane. The opposite patterns are characterized for the AV_S. Therefore the concave shapes are possibly attributed to different propagating directions between P- and S-waves. The calculations of seismic properties were conducted with every 10% step. —, AV_P in Gln-rich layer; - -, AV_P in Lws-rich layer; —, AV_S in Gln-rich layer; **- -**, AV_S in Lws-rich layer.

CONCLUSIONS

In summary, we investigated fabric analyses of a Diablo Range blueschist, which preserves two distinctive layers mostly composed of glaucophane and lawsonite. Results show higher aspect ratios, lower angles to the foliation, and higher fabric strengths for glaucophane in the representative two layers, advocating strain partitioning into the glaucophane-rich layer (GRL) rather than the lawsonite-rich layer (LRL), and also indicating the weakness of glaucophane against deformation compared with lawsonite. To conclude, our discovery supports the idea that glaucophane mainly manages rheology and seismic anisotropy of subducting oceanic crusts.

ACKNOWLEDGEMENTS

The authors appreciate the assistance of H. Rehman, Y. Soda and H. Yamamoto for constructive comments, and K. Okamoto for editing. We are also grateful to Y. Shibata and L.F.G. Morales for technical support on the EPMA analyses and seismic property calculations, respectively. This project has been supported by the Japan Society for the Promotion of Science (JSPS) to IK (No. 21684030), KM (No. 22244062) and TT (No. 22654058).

REFERENCES

BEZACIER L., REYNARD B., BASS J. D., WANG J. & MAINPRICE D. 2010. Elasticity of glaucophane, seismic velocities and anisotropy of the subducted oceanic crust. *Tectonophysics* **494**, 201–10.

CARTER N. L. & AVÉ LALLEMANT H. G. 1970. High temperature deformation of dunite and peridotites. *Geological Society of America Bulletin* **81**, 2181–202.

COLEMAN R. G. 1980. Tectonic inclusions in serpentinite. *Archives des Sciences, Société de Physique et d'Histoire Naturelle de Genève* **33**, 89–102.

COLEMAN R. G. 1996. New Idria Serpentinite: A land management dilemma. *Environmental & Engineering Geoscience* **2**, 9–22.

CUMBEST R. J., DRURY M. R., VAN ROERMUND H. L. M. & SIMPSON C. 1989. Dynamic recrystallization and chemical evolution of clinoamphibole from Senja Norway. *Contributions to Mineralogy and Petrology* **101**, 339–49.

DÍAZ ASPIROZ M., LLOYD G. E. & FERNÁNDEZ C. 2007. Development of lattice preferred orientation in clinoamphiboles deformed under low-pressure metamorphic conditions. A SEM/EBSD study of metabasites from the Aracena metamorphic belt (SW Spain). *Journal of Structural Geology* **29**, 629–45.

DRURY M. R. & URAI J. L. 1990. Deformaton-related recrystallization processes. *Tectonophysics* **172**, 235–53.

EBERT A., HERWEGH M. & PFIFFNER A. 2007. Cooling induced strain localization in carbonate mylonites within a large-scale shear zone (Glarus thrust, Switzerland). *Journal of Structural Geology* **29**, 1164–84.

EVANS B., RENNER J. & HIRTH G. 2001. A few remarks on the kinetics of static grain growth in rocks. *International Journal of Earth Sciences* **90**, 88–103.

FUJIMOTO Y., KONO Y., HIRAJIMA T., KANAGAWA K., ISHIKAWA M. & ARIMA M. 2010. P-wave velocity and anisotropy of lawsonite and epidote blueschists: Constraints on water transportation along subducting oceanic crust. *Physics of the Earth and Planetary Interiors* **183**, 219–28.

ILDEFONSE B., LARDEAUZ J.-M. & CARON J.-M. 1990. The behavior of shape preferred orientations in metamorphic rocks: Amphiboles and jadeites from the Monte Mucrone area (Sesia-Lanzo zone, Italian Western Alps). *Journal of Structural Geology* **12**, 1005–11.

IMON R., OKUDAIRA T. & KANAGAWA K. 2004. Development of shape- and lattice-preferred orientations of amphibole grains during initial cataclastic deformation and subsequent deformation by dissolution–precipitation creep in amphibolites from the Ryoke metamorphic belt, SW Japan. *Journal of Structural Geology* **26**, 793–805.

ISMAÏL W. B. & MAINPRICE D. 1998. An olivine fabric database: An overview of upper mantle fabrics and seismic anisotropy. *Tectonophysics* **296**, 145–57.

JUNG H. & KARATO S.-I. 2001. Water-induced fabric transitions in olivine. *Science* **293**, 1460–3.

JUNG H., KATAYAMA I., JIANG Z., HIRAGA T. & KARATO S. 2006. Effect of water and stress on the lattice-preferred orientation of olivine. *Tectonophysics* **421**, 1–22.

LEAKE B. E., WOOLLEY A. R., ARPS C. E. S. *et al.* 1997. Nomenclature of amphiboles; Report of the Subcommittee on Amphiboles of the International Mineralogical Association, Commission on New Minerals and Mineral Names. *Canadian Mineralogist* **35**, 219–46.

MAINPRICE D. & SILVER P. G. 1993. Interpretation of SKS-waves using samples from the subcontinental lithosphere. *Physics of the Earth and Planetary Interiors* **78**, 257–80.

MAINPRICE D., BARRUOL G. & BEN ISMAÏL W. 2000. The anisotropy of the Earth's mantle: From single crystal to polycrystal. *In* Karato S., Forte A. M., Liebermann R. C., Masters G. and Stixrude L. (eds.) *Mineral Physics and Seismic Tomography: From Atomic to Global*, Geophysical Monograph 117, pp. 237–64, AGU, Washington, DC.

MARUYAMA S. & LIOU J. G. 1988. Petrology of Franciscan metabasites along the jadeite-glaucophane

type facies series, Cazadero, California. *Journal of Petrology* **29**, 1–37.

MARUYAMA S., CHO M. & LIOU J. G. 1986. Experimental investigations of blueschist-greenschist transition equilibria: Pressure dependence of Al2O3 contents in sodic amphiboles – A new barometer. *In* Evans B. W. and Brown E. H. (eds.) *Blueschist and Eclogite*, Geological Society of America Memoir, 164, pp. 1–16, The Geological Society of America Inc., Colorado.

MEZGER J. E. 2010. Rotation of irregular staurolite porphyroblasts in a simple shear dominated shear zone controlled by initial growth orientation and aspect ratio. *Journal of Structural Geology* **32**, 1147–57.

NYMAN M. W., LAW R. D. & SMELIK E. 1992. Cataclastic deformation for the development of core mantle structures in amphibole. *Geology* **20**, 455–8.

REYNARD B., GILLET P. & WILLAIME C. 1989. Deformation mechanisms in naturally deformed glaucophanes: A TEM and HREM study. *European Journal of Mineralogy* **1**, 611–24.

SIEGESMUND S., HELMING K. & KRUSE R. 1994. Complete texture analysis of a deformed amphibolite: Comparison between neutron, diffraction and U-stage data. *Journal of Structural Geology* **16**, 131–42.

SINOGEIKIN S. V. & BASS J. D. 2000. Single-crystal elasticity of pyrope and MgO to 20 GPa by Brillouin scattering in the diamond cell. *Physics of the Earth and Planetary Interiors* **120**, 43–62.

SKEMER P., KATAYAMA I., JIANG Z. & KARATO S. 2005. The misorientation index: Development of a new method for calculating the strength of lattice-preferred orientation. *Tectonophysics* **411**, 157–67.

TEYSSIER C., WHITNEY D. L., TORAMAN E. & SEATON N. C. A. 2010. Lawsonite vorticity and subduction kinematics. *Geology* **38**, 1123–6.

TSUJIMORI T., SISSON V. B., LIOU J. G., HARLOW G. E. & SORENSEN S. S. 2006. Very-low-temperature record in subduction process: A review of worldwide lawsonite eclogites. *Lithos* **92**, 609–24.

TSUJIMORI T., LIOU G. J. & COLEMAN R. G. 2007. Finding of high-grade tectonic blocks from the New Idria serpentinite body, Diablo Range, California: Petrologic constraints on the tectonic evolution of an active serpentinite diapir. *In* Cloos M., Carlson W. D., Gilbert M. C., Liou J. G. and Sorensen S. S. (eds.) *Convergent Margin Terranes and Associated Regions: A Tribute to W. G. Ernst*, Geological Society of America, Special Papers 419, pp. 67–80.

WHITNEY D. L. & EVANS B. W. 2010. Abbreviations for names of rock-forming minerals. *American Mineralogist* **95**, 185–7.

ZUCALI M., CHATEIGNER D., DUGNANI M., LUTTEROTTI L. & OULADDIAF B. 2002. Quantitative texture analysis of glaucophanite deformed under eclogite facies conditions (Sesia-Lanzo Zone, Western Alps): Comparison between X-ray and neutron diffraction analysis. *Geological Society, London* **200**, 239–53.